

## Supplementary Materials for

### **A Paravascular Pathway Facilitates CSF Flow Through the Brain Parenchyma and the Clearance of Interstitial Solutes, Including Amyloid $\beta$**

Jeffrey J. Iliff,\* Minghuan Wang, Yonghong Liao, Benjamin A. Plogg, Weiguo Peng, Georg A. Gundersen, Helene Benveniste, G. Edward Vates, Rashid Deane, Steven A. Goldman, Erlend A. Nagelhus, Maiken Nedergaard\*

\*To whom correspondence should be addressed. E-mail: jeffrey\_iliff@urmc.rochester.edu (J.J.I.); nedergaard@urmc.rochester.edu (M.N.)

Published 15 August 2012, *Sci. Transl. Med.* **4**, 147ra111 (2012)  
DOI: 10.1126/scitranslmed.3003748

#### **This PDF file includes:**

##### Methods

Fig. S1. Quantification of fluorescent CSF tracer distribution within the brain parenchyma.

Fig. S2. Measurement of subarachnoid CSF entry into the brain parenchyma.

Fig. S3. In vivo imaging of para-arterial influx of small- and large-molecular weight tracers.

Fig. S4. CSF does not enter the brain parenchyma along paravenous pathways.

Fig. S5. Intracisternally and intraparenchymally injected tracer shares the same paravenous drainage pathway.

Fig. S6. Visualization of paravascular accumulation of tracer and the Virchow-Robin space in wild-type and *Aqp4*-null mice.

Fig. S7. Differential expression of AQP4 in periarterial versus perivenous astrocytes.

Fig. S8. Measurement of interstitial solute clearance from the brain.

Fig. S9. Schematic diagram of paravascular and interstitial bulk flow pathways.

#### **Other Supplementary Material for this manuscript includes the following:**

(available at

[www.sciencetranslationalmedicine.org/cgi/content/full/4/147/147ra111/DC1](http://www.sciencetranslationalmedicine.org/cgi/content/full/4/147/147ra111/DC1))

Movie S1 (.avi format). Direct visualization of para-arterial influx of subarachnoid CSF tracer into the brain parenchyma.

Movie S2 (.avi format). Animation depicting the role of paravascular CSF influx in interstitial solute clearance from the brain.

## Supplementary Methods

### *Animals*

All experiments were approved by the University Committee on Animal Resources of the University of Rochester Medical Center. Unless otherwise noted, 8-12 week old male C57BL/6 mice (Charles River) were used in experiments. To visualize perivascular astrocytic endfeet, FVB/N-Tg(GFAPGFP)14Mes/J (GFAP-GFP, JAX) mice were used. These mice overexpress green fluorescent protein under the control of the astrocyte-specific GFAP promoter. To define the paravascular route of CSF tracer influx and efflux, a transgenic double reporter mouse was generated. Tg(TIE2GFP)287Sato/J (Tie2-GFP, JAX) were crossed with NG2DsRedBAC(54) (NG2-DsRed, JAX). Tie2-GFP mice overexpress green fluorescent protein under the endothelium-specific Tie2 promoter, while NG2-DsRed mice express the red fluorescent protein DsRed under the control of the NG2 promoter. Although the NG2-DsRed mice were initially generated to study NG2-positive glial cells, adult animals also express DsRed in brain pericytes and vascular smooth muscle cells. In Tie2-GFP:NG2-DsRed animals, all blood vessels are labeled with GFP (in the endothelial cell layer). Capillaries (Fig. 3F), veins (Fig. 3H) and venules (Fig. 3G) express low levels of punctuate DsRed (in pericytes and disperse vascular smooth muscle cells), while arteries (Fig. 3D-E) and arterioles (Fig. 3A-C) exhibit a dense circumferential pattern of DsRed labeling. This allows arteries and arterioles to be readily distinguished from veins and venules (Fig. 3A, Fig. S4) without the need of additional histochemical labeling. *Aqp4*<sup>-/-</sup> (*Aqp4*-null) mice were generated as described (53). These animals are global *Aqp4* gene knockouts backcrossed onto a C57BL/6 background.

### *CSF Tracers*

All fluorescent CSF tracers were constituted in artificial CSF at a concentration of 0.5%. This includes ALEXA-594 hydrazide (A594), FITC-dextran 2000 (FITC-d2000), Texas Red-dextran 3 (TR-d3), Texas Red-dextran 2000 (TR-d2000), ovalbumin-conjugated ALEXA-647 (OA-647) (all from Invitrogen). HiLyte555-conjugated amyloid  $\beta_{1-40}$  (Anaspec) was constituted in artificial CSF at a concentration of 0.1%. Radio-labeled <sup>3</sup>H-mannitol (15-30Ci/mmol, Perkin Elmer) was dissolved in artificial CSF at a 0.1  $\mu$ Ci/ $\mu$ l. Radio-labeled <sup>3</sup>H-dextran 10 (100-500mCi/g, American Radiolabeled Chemicals) was dissolved in artificial CSF at 0.01  $\mu$ Ci/ $\mu$ l. Radio-labeled <sup>125</sup>I-amyloid  $\beta_{1-40}$  (2200Ci/mmol, Perkin Elmer) was dissolved in artificial CSF at 0.005  $\mu$ Ci/ $\mu$ l (2.3nmol/L).

### *Ventriculo-cisternal perfusion*

Anesthetized mice were fixed in a stereotaxic frame and a 33GA steel needle was stereotactically inserted via a small burr hole into the right lateral ventricle (0.95mm lateral, 2.35mm ventral and 0.22mm caudal to bregma). A second 30GA needle was inserted into the cisterna magna. Closed ventriculo-cisternal perfusion was conducted by infusing tracer dissolved in artificial CSF into the lateral ventricle and withdrawing CSF from the cisterna magna at an equal rate of 200nl/min with a coupled syringe pump (Micro4, WPI).

For evaluating the distribution of tracer into the brain parenchyma, animals were trans-cardially perfused with 4% paraformaldehyde (PFA), post-fixed overnight, and 100 $\mu$ m slices were cut on a vibratome and mounted with PROLONG Anti-Fade Gold

with DAPI (Invitrogen). Tracer penetration from the ventricular compartment was imaged *ex vivo* by epifluorescence microscopy or laser scanning confocal microscopy.

#### *Intracisternal tracer injection*

Anesthetized mice were fixed in a stereotaxic frame and a 30GA needle was inserted into the cisterna magna. For intracisternal injections, 10 $\mu$ l of CSF tracer was injected at a rate of 2 $\mu$ l/min over 5 minutes with a syringe pump (Harvard Apparatus).

To visualize tracer movement from the subarachnoid space of the cisterna magna into the brain parenchyma, animals were perfusion fixed between 30 minutes and 6 hours after intracisternal tracer injection. 100 $\mu$ m vibratome slices were cut and mounted as above and tracer movement was imaged *ex vivo* by epifluorescence microscopy or laser scanning confocal microscopy.

To evaluate the absolute proportion of subarachnoid CSF that enters the brain (Fig. S2), we first injected either radio-labeled  $^3\text{H}$ -mannitol (1.0 $\mu$ Ci in 10 $\mu$ l) or  $^3\text{H}$ -dextran-10 (0.1 $\mu$ Ci in 10 $\mu$ l) intracisternally into anesthetized animals. After 15, 30 or 45 minutes, animals were rapidly decapitated, the skull opened, the dura removed and the brain harvested. The brain was solublized in 2ml Soluene (Sigma) at 45 $^{\circ}$ C overnight. 10ml Hionic Fluor liquid scintillation cocktail (Perkin Elmer) was added and radioactivity was measured in a Multipurpose Scintillation Counter (Beckman Coulter). Brain radioactivity was normalized to total radioactivity detected in a 10 $\mu$ l aliquot put directly into a scintillation vial immediately before intracisternal radio-tracer injection and expressed as the % of total injected radioactivity.  $^3\text{H}$ -mannitol and  $^3\text{H}$ -dextran accumulation in the brain was compared by 2-way ANOVA with Bonferroni's post-hoc test. Approximate maximal  $^3\text{H}$ -mannitol influx was determined by fitting the accumulation curve to a one-phase association function, then determining the plateau value for the best fit curve ( $39.96 \pm 5.55\%$ ,  $R^2 = 0.3597$ ).

#### *Ex vivo fluorescence imaging*

Tracer penetration into the brain was evaluated *ex vivo* by epifluorescence microscopy. Multi-channel whole-slice montages were acquired with the Virtual Slice module of StereoInvestigator Software (Microbrightfield). This included separate DAPI, Green and Red emission channels. Exposure levels were determined based upon un-injected control slices, then maintained constant throughout the study.

To quantify tracer movement into fixed slices, slice images were analyzed in ImageJ software (NIH, Fig. S1). For each slice, color channels were split and a whole-slice region of interest (ROI) was defined based upon the DAPI channel. The color channels corresponding to each tracer were background subtracted based upon an ROI outside of the slice area. The mean slice fluorescence intensity was calculated, then the slice was uniformly thresholded at a pixel intensity of 75 (out of 255) and the thresholded area expressed as a % of overall slice area. Approximately 10-14 slices per animal were imaged in this manner, and mean fluorescence intensity and tracer coverage between slices was averaged within each animal to generate a single biological replicate. The effect of tracer size upon fluorescence intensity or tracer distribution was evaluated by one-way ANOVA with Tukey's post-hoc test to determine differences between individual tracers. The effect of *Aqp4* gene deletion upon tracer influx into the brain was evaluated by 2-way ANOVA with Bonferroni's post-hoc test to

determine differences at individual time points.

Tracer movement into and through fixed vibratome slices was additionally imaged at high power by laser scanning confocal microscopy (FV500, Olympus) with FluoView (Olympus) software. Images were processed with ImageJ Software (NIH) with the UCSD plugin set.

#### *In vivo 2-photon laser scanning microscopy*

For in vivo imaging, anesthetized animals were intubated and artificially ventilated with room air using a small animal ventilator (CWE) at ~100 breaths/min and tidal volume of 0.3-0.4ml. Body temperature was kept at 37°C with a temperature-controlled warming pad. A craniotomy (3mm in diameter) was made over the cortex 1mm lateral and 0.5mm posterior to bregma. The dura was left intact and the craniotomy was covered with aCSF and sealed with a glass coverslip. The femoral artery was cannulated for mean arterial blood pressure monitoring and the measurement of arterial blood gas values. Only mice with blood gases within the physiological range ( $pO_2 = 80-150\text{mmHg}$ , pH 7.25-7.5) were included in the present study. To visualize the vasculature, 0.1ml BBB-impermeable Cascade Blue-dextran 10 (MW 10kD) or Texas Red-dextran 70 (MW 70kD; both 1% in saline, Invitrogen) was injected intra-arterially immediately before imaging.

A Mai Tai laser (SpectraPhysics) attached to a confocal scanning system (Fluoview 300, Olympus) and an upright microscope (IX51W, Olympus) was used for in vivo imaging as described (55). A 20X (0.9NA) water immersion lens was used to image the cortex, from the surface to a depth of ~250 $\mu\text{m}$ . Excitation wavelength was 800 for Cascade Blue and 870nm for GFP, FITC and Texas Red. For GFP, FITC and Texas Red, emission was collected at 575-645nm. The cerebral vasculature was first imaged with 512 x 512 pixel frames from the surface to a depth of 240 $\mu\text{m}$  with 5 $\mu\text{m}$  z-steps. After intracisternal injection of CSF tracer, tracer movement into the cortex was conducted with dual-channel (FITC and Texas Red) 512 x 512 pixel image acquisition. The cortex was repeatedly scanned from the surface to 240 $\mu\text{m}$  below the surface with 20 $\mu\text{m}$  z-steps at 1 minute intervals for the duration of the experiment. Image analysis was conducted in with ImageJ software (NIH) with the UCSD plugin set. After imaging, penetrating arterioles were distinguished from penetrating venules on the basis of morphology: surface arteries passing superficially to surface veins and exhibiting less branching at superficial cortical depths. Imaging planes 100-120 $\mu\text{m}$  below the cortical surface were selected for the analysis of intracisternal tracer penetration. To define para-vascular tracer movement, a circular ROI 25 pixels in diameter was defined surrounding three penetrating arterioles and ascending venules. To define tracer movement into para-vascular brain tissue, donut-shaped ROIs were defined that had an external diameter of 150 pixels and an internal diameter of 50 pixels (thus excluding the paravascular ROI). These were centered upon the penetrating arterioles and ascending venules. Mean pixel intensity within these ROIs was measured at each time point. Within each animal at each time point para-arteriolar and paravenous ROIs were separately averaged to generate values for a single biological replicate. When tracer movement along penetrating arterioles or ascending veins, or into para-arteriolar and paravenous brain tissue was compared, a 2-way ANOVA was used followed by Bonferroni's post-hoc test. The same test was used to evaluate the effect of *Aqp4* gene

deletion on tracer movement along paravascular spaces or into paravascular brain tissue.

#### *Intraparenchymal tracer injection*

To evaluate the pathways and rates of interstitial fluid and solute clearance from the brain, fluorescent and radio-labeled tracers were injected stereotactically into the brain parenchyma. Anesthetized animals were fixed in a stereotaxic frame and a 33GA needle was inserted via a small burr hole into the brain at the following coordinates: intra-cortical injections (0.22mm caudal, 2.0mm lateral, 1.75mm ventral to bregma), intra-striate injections (0.22mm caudal, 2.5mm lateral, 3.5mm ventral to bregma), intra-thalamic injections (1.82mm caudal, 1.25mm lateral, 3.75mm ventral to bregma). After needle insertion, 30 minutes was allowed to elapse to allow the needle track to swell closed. 1.0 $\mu$ l of tracer (dissolved in artificial CSF) was injected at a rate of 17nl/min.

When the distribution of intra-parenchymal fluorescent tracer (OA-647) was evaluated, animals were perfusion-fixed for 1-3h after injection and vibratome slices were imaged by laser scanning confocal microscopy. To define the pathways of HiLyte-555-amyloid  $\beta_{1-40}$  clearance from the brain after intra-striate injection, fixed vibratome sections were imaged by laser scanning confocal microscopy.

When we evaluated the absolute rate of interstitial solute clearance from the brain,  $^3\text{H}$ -mannitol,  $^3\text{H}$ -dextran-10 or  $^{125}\text{I}$ -amyloid  $\beta_{1-40}$  was injected into the striatum (Fig. S8). 15min, 30min, 1h or 2h later, the animal was rapidly decapitated and the brain harvested. The brain was solublized as above, and the radioactivity present in the brain was measured by liquid scintillation spectrometry. All radioactivity values were normalized to 1 $\mu$ l injection standards taken immediately prior to each intra-parenchymal injection. The effect of *Aqp4* gene deletion upon  $^3\text{H}$ -mannitol,  $^3\text{H}$ -dextran-10 or  $^{125}\text{I}$ -amyloid  $\beta_{1-40}$  clearance from the brain was evaluated with a 2-way ANOVA and Bonferroni's post-hoc test to determine differences at individual time points.

#### *Immunofluorescence*

Free-floating immunofluorescence was conducted on 100 $\mu$ m PFA-fixed vibratome slices. Slices were blocked for 1h at room temperature with 3% normal donkey serum (Jackson ImmunoResearch), incubated with primary antibody overnight at 4 $^{\circ}\text{C}$  and incubated with secondary antibody for 2 hours at room temperature. Primary antibodies included rat anti-CD31 (an endothelial marker; 1:200, Abcam), mouse anti-GFAP (an astrocytic marker; 1:500, Millipore) and rabbit anti-AQP4 (1:500, Millipore). Secondary antibodies included Cy2-conjugated donkey anti-rat, Cy5-conjugated donkey anti-mouse and Cy3-conjugated donkey anti-rabbit (Jackson ImmunoResearch).

#### *Preembedding light and electron microscopic cytochemistry*

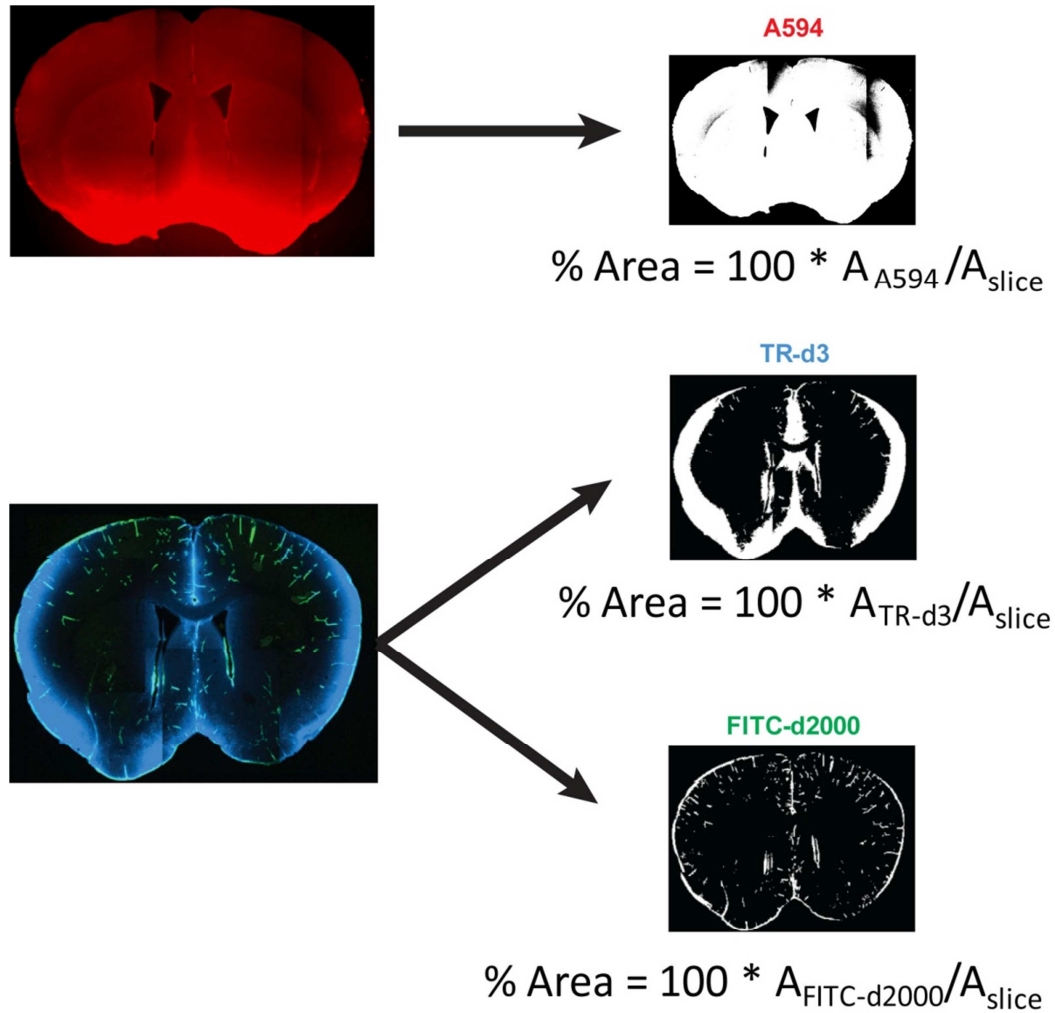
Wild type and *Aqp4*-null mice were injected with FITC-d40 and fixed after 5 minutes by transcardiac perfusion with 4% formaldehyde and 0.1% glutaraldehyde in 0.1M phosphate buffer (pH 7.4). Brains were post-fixed overnight and cut in 100 $\mu$ m coronal sections by a vibratome. Free-floating sections were incubated with HRP-conjugated anti-fluorescein antibodies (Abcam, Cat: AB6656, 5 $\mu$ g/ml) for 24 h (4 $^{\circ}\text{C}$ ) and then subjected to the diaminobenzidine (DAB)-peroxidase procedure to visualize the fluorescein tracer, as described (56). Light microscopy images of the sections were

acquired before areas of the parietal cortex were dissected and embedded in Durcupan (56). Ultrathin sections (~90 nm) were cut on a Reichert ultramicrotome. Finally, the sections were counterstained and examined in a FEI Tecnai 12 transmission electron microscope. Digital images were recorded at a nominal magnification of x26000.

*Electron microscopic morphological analysis*

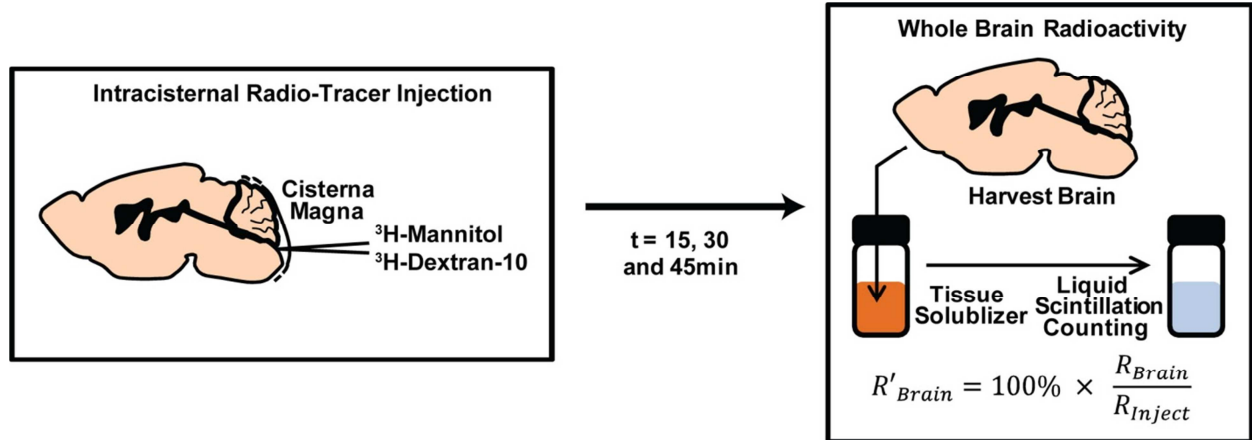
Wild type ( $n=3$ ) and *Aqp4*-null mice ( $n=4$ ) were fixed by transcardiac perfusion with 2.5% glutaraldehyde and 1% formaldehyde in 0.1M phosphate buffer (pH 7.4, 9ml/min for 25 min). Brains were post-fixed overnight before 300-500 $\mu$ m coronal sections were dissected and embedded in Durcupan (55). Ultrathin sections were cut, counterstained, and examined as described above. Digital images of penetrating vessels were recorded at a nominal magnification of x4200. Maximal width of the Virchow-Robin space was measured around penetrating vessels at a minimum depth 80 $\mu$ m from the pial surface (range: 166-415 $\mu$ m and 83-366 $\mu$ m for wild type and *Aqp4*-null mice, respectively).

**Fig. S1. Quantification of fluorescent CSF tracer distribution within the brain parenchyma.**



After injection of intracisternal A594, TR-d3 and FITC-d2000 injections, animals were perfusion fixed and 100- $\mu\text{m}$  vibratome sections cut. Slices were imaged by epifluorescence microscopy at 4X and montages generated. To evaluate tracer coverage, the color channels were separated, the images background subtracted, uniformly thresholded and the thresholded area was calculated and expressed as a percentage of overall slice area.

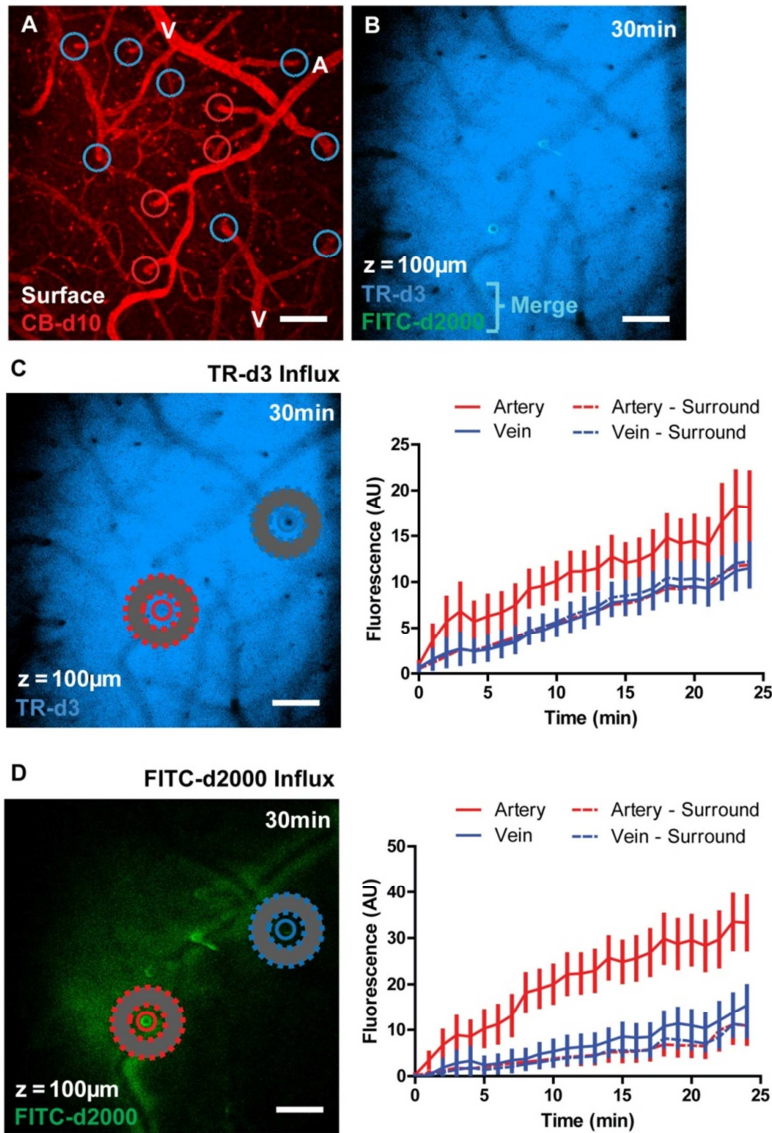
**Fig. S2. Measurement of subarachnoid CSF entry into the brain parenchyma.**



Schematic diagram depicting the measurement of subarachnoid CSF entry into the brain parenchyma.  $^3\text{H}$ -Mannitol,  $^3\text{H}$ -Dextran-10 or  $^{125}\text{I}$ -A $\beta_{1-40}$  was injected intracisternally. To quantify radiotracer accumulation within the brain parenchyma, the brain was harvested 15, 30 or 45 min after radio-tracer injection. Brains were solublized in Soluene, and then total brain radioactivity was measured by liquid scintillation counting. The proportional brain radioactivity ( $R'_{Brain}$ ) was calculated based upon the total measured brain radioactivity ( $R_{Brain}$ ) and the total injected radioactivity ( $R_{Inject}$ ). During harvest, the dura was removed from the brain. Thus the brain homogenate does not include radio-tracer remaining in the subarachnoid CSF compartment.



**Figure S3. In vivo imaging of para-arterial influx of small- and large-molecular weight tracers.**

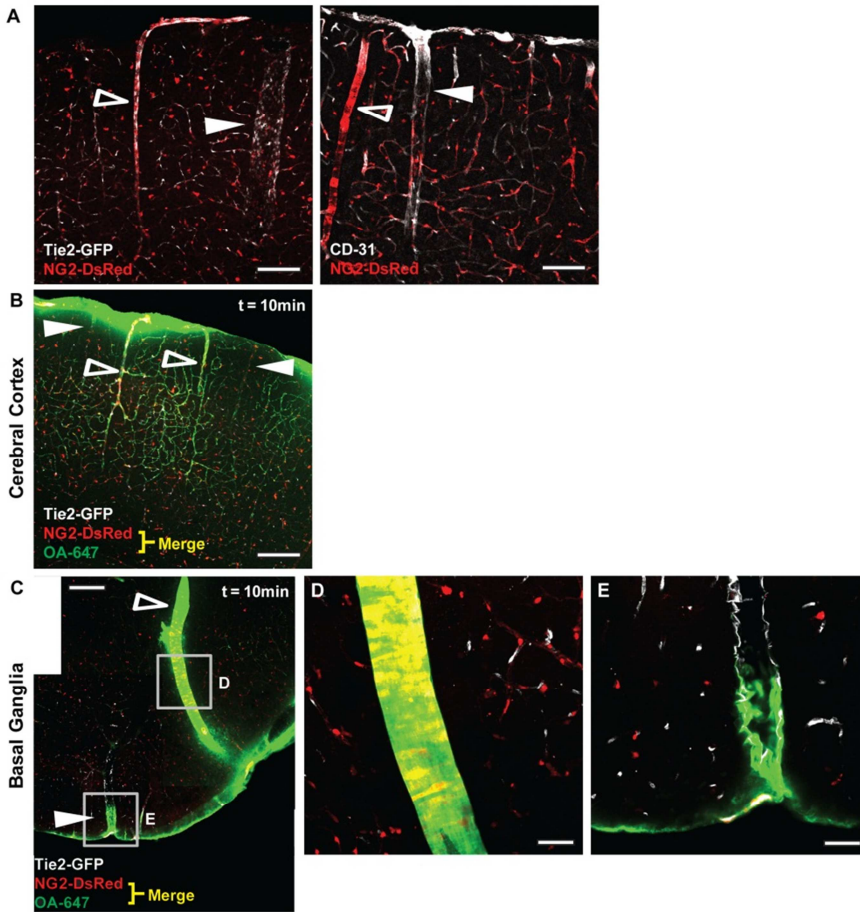


The movement of two dextrans of differing molecular weight (TR-d3 and FITC-d2000) along para-arterial pathways and into the cortical interstitium was imaged in anesthetized mice by in vivo 2-photon laser scanning microscopy within a closed cranial window. **(A)** The cerebral vasculature was visualized with intra-arterial Cascade Blue-dextran-10 (CB-d10) and penetrating arterioles (A) and veins (V) were identified morphologically (red and blue circles, respectively). **(B-D)** The movement of small and large molecular weight tracer along para-arterial and paravenous pathways was evaluated by measuring the mean fluorescence intensity within circular ROIs centered on penetrating vessels. The movement of tracer into the surrounding interstitium was defined by measuring mean

fluorescence intensity in donut-shaped ROIs centered upon penetrating vessels (red and blue dashed donuts). **(C)** Small molecular weight tracer moved readily from the para-arterial space (red solid line) into the para-arterial (red dashed line) and paravenous (blue dashed line) interstitium. The lack of a statistically-significant difference ( $P = 0.056$ ,  $n=6$  each group) between the curves indicates that this tracer enjoys relatively unrestricted movement outward from the para-arterial space. **(D)** Large molecular weight tracer moved readily into the cortex along penetrating arterioles (solid red line) but not along penetrating venules (solid blue line;  $*P<0.01$ ,  $n= 6$  each group). Tracer intensity measured in the tissue surrounding penetrating arterioles and veins (dashed red and blue line, respectively) remained at the same low levels observed for paravenous spaces. Thus, large molecular weight tracer remains confined primarily to

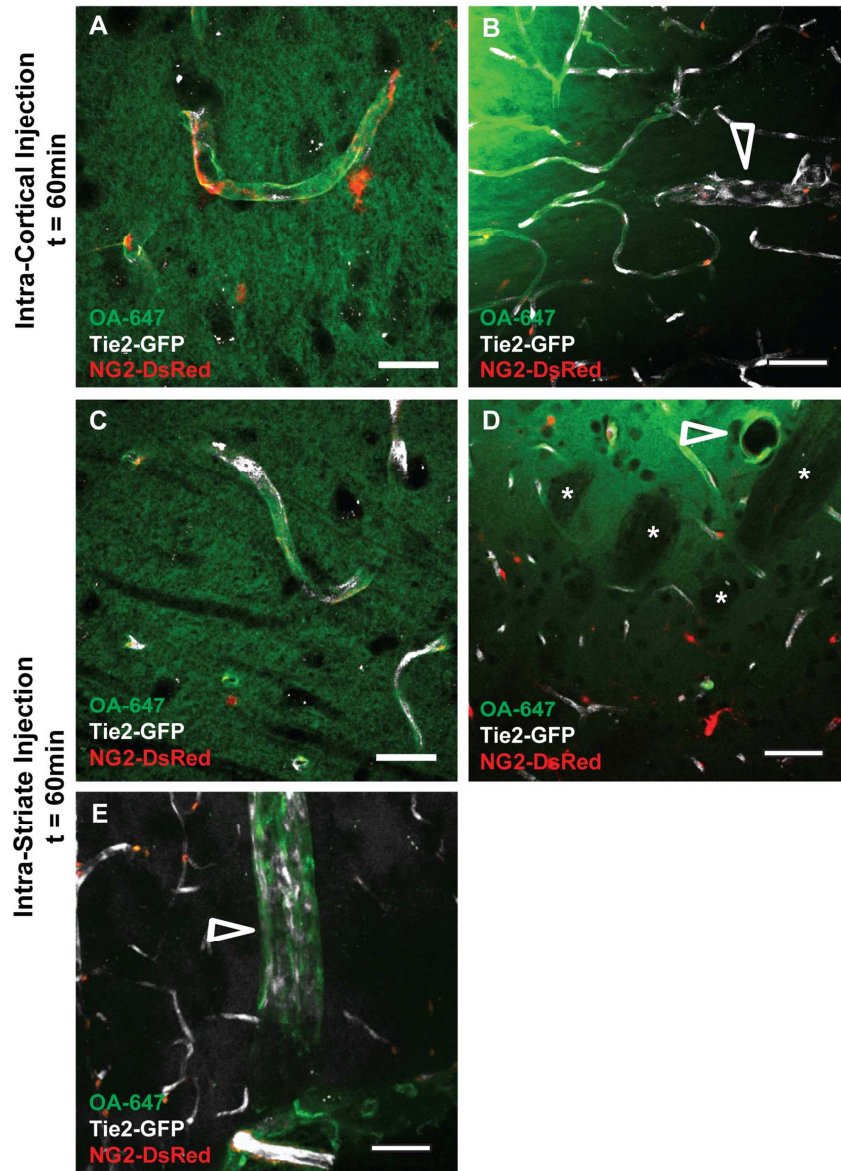
para-arterial spaces and does not readily enter the brain interstitium. Scale bars: 100 $\mu$ m.

**Figure S4. CSF does not enter the brain parenchyma along paravenous pathways.**



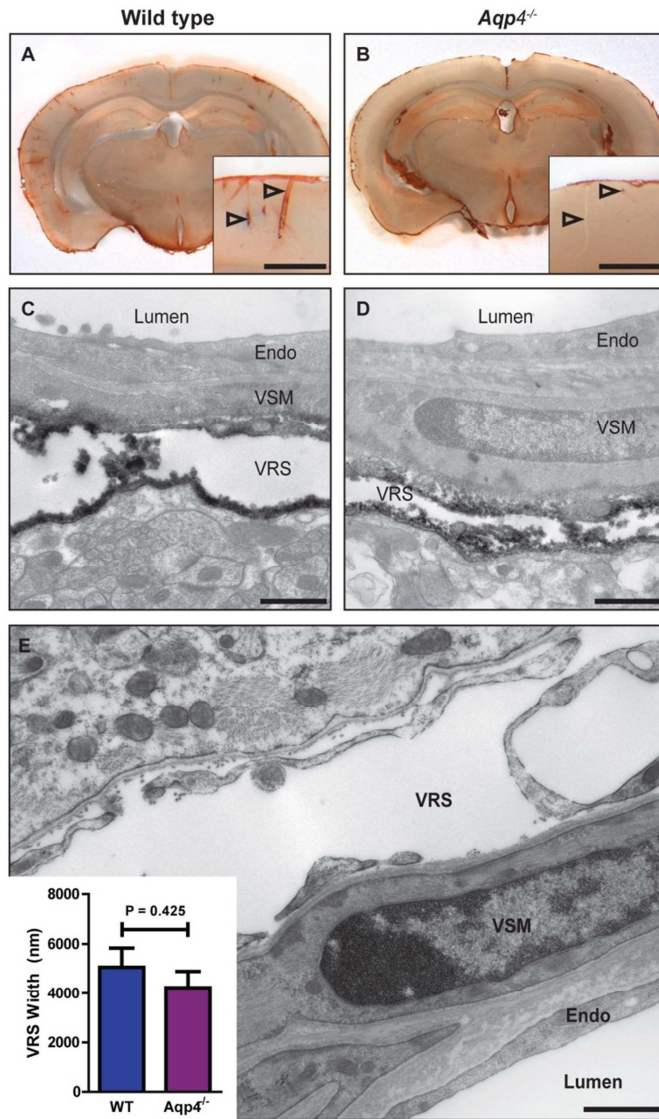
To evaluate para-arterial versus paravenous subarachnoid CSF tracer influx, OA-647 was injected intracisternally into Tie2-GFP:NG2-DsRed double reporter mice. **(A)** In these mice, the endothelium of all blood vessels is labeled with GFP while vascular smooth muscle cells and pericytes are labeled with DsRed. Thus arteries and arterioles (empty arrowheads) are easily distinguished by the presence of distinct circumferential DsRed labeling, while veins (filled arrowheads) lack such labeling. The arterial specificity of NG2-DsRed labeling is seen when brain slices from NG2-DsRed mice are labeled with the endothelial marker CD-31 (right). **(B)** In the cerebral cortex, intracisternal tracer enters the brain along DsRed<sup>+</sup> penetrating arterioles but not along DsRed<sup>-</sup> veins. Distal venous labeling is seen at times, but typically originates from a para-arteriolar inflow path via the intervening capillary bed. **(C-E)** Large vessels along the ventral brain surface exhibit the same pattern. Paravascular spaces surrounding large perforating arteries (empty arrowheads, D) move large fluxes of CSF tracer into the parenchyma, while tracer does not substantially penetrate into the parenchyma along basal draining veins (filled arrow heads, E). Scale bars: 100 $\mu$ m (B, C), 50 $\mu$ m (A), 20 $\mu$ m (D-E).

**Figure S5. Intracisternally and intraparenchymally injected tracer shares the same paravenous drainage pathway.**



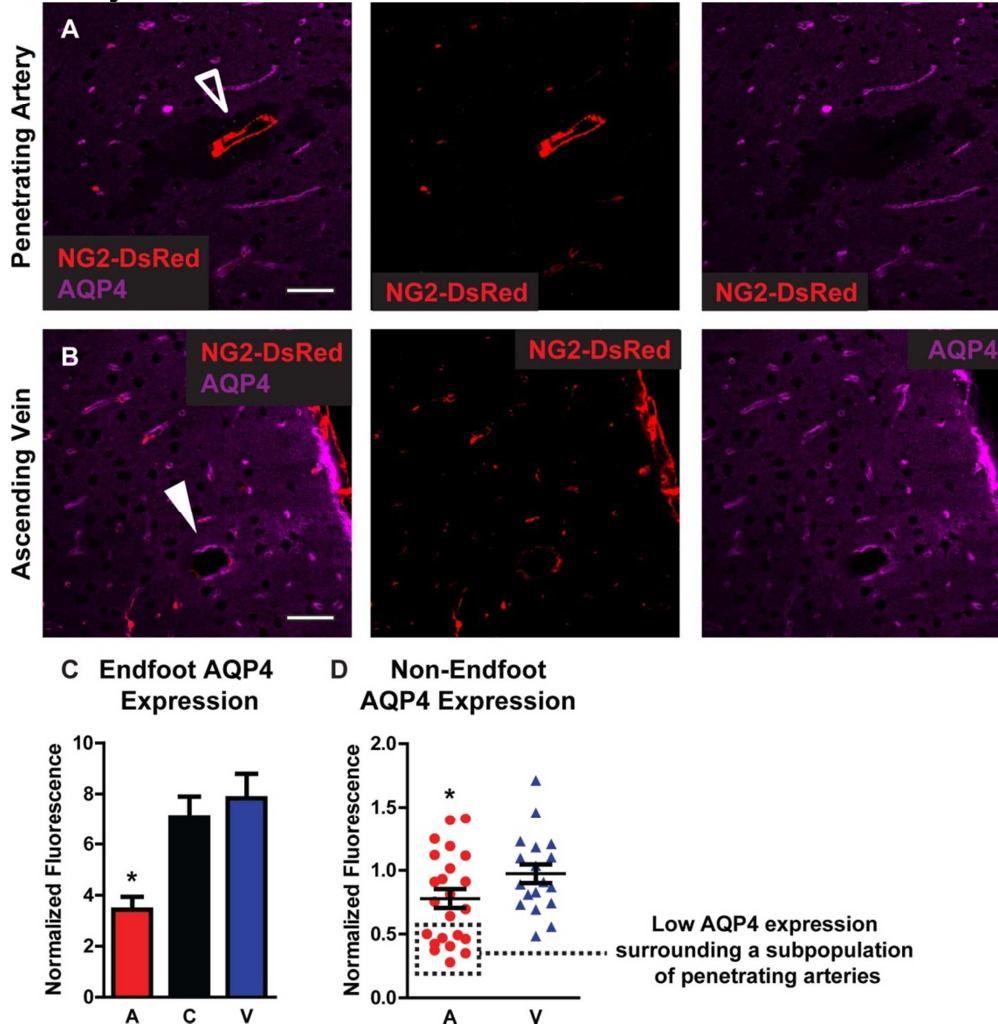
Tie2-GFP:NG2-DsRed double reporter mice were injected intra-parenchymally with OA-647. **(A-B)** Intracortically-injected tracer accumulated around the microvasculature, and moved outward from the injection site most rapidly along para-capillary and para-venous (arrowheads) pathways. **(C-D)** Intra-striate tracer similarly accumulated around capillaries and venules. Tracer that was injected into gray matter was excluded from white matter bundles (asterisks, D). **(E)** Intra-parenchymal tracer was cleared from the brain primarily along the internal cerebral and caudal rhinal veins, although lesser clearance along cortical ascending veins and venules was also observed. Scale bars: 50µm (B, D-E), 20µm (A, C).

**Figure S6. Visualization of paravascular accumulation of tracer and the Virchow-Robin space in wild type and *Aqp4*-null mice.**



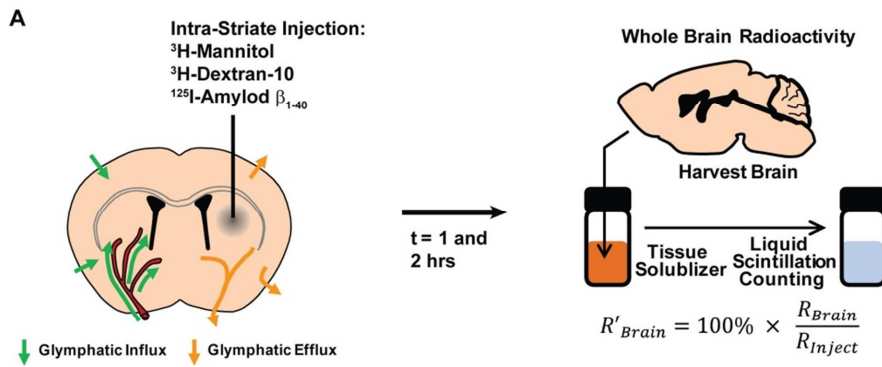
**(A-B)** Intracisternally injected FITC-d40 was visualized by DAB immunohistochemistry. 5 minutes after injection, reaction product is evident along penetrating cortical vessels (arrows in inset) of wild type animals (A). Labeling intensity around vessels is much weaker in *Aqp4*-null animals (B). Insets show labeling in parietal cortex at high magnification. **(C-D)** Electron micrographs showing the electron dense DAB reaction product in the proximal paravascular space (Virchow-Robin space, VRS) surrounding penetrating cortical arterioles. Compared to wild type animals **(C)**, the VRS in *Aqp4*-null animals **(D)** appears ultrastructurally intact. **(E)** VRS of an un.injected *Aqp4*-null animal visualized ~1000  $\mu\text{m}$  below the cortical surface. Inset shows width of VRS around penetrating vessels (n=10 for wild type animals, n=11 for *Aqp4*-null animals; values are mean  $\pm$  SEM). Endo, endothelial cell; VSM, vascular smooth muscle cell. Scale bars: 500  $\mu\text{m}$  (insets in A and B), 1  $\mu\text{m}$  (C-E).

**Figure S7. Differential expression of AQP4 in periarterial versus perivenous astrocytes.**

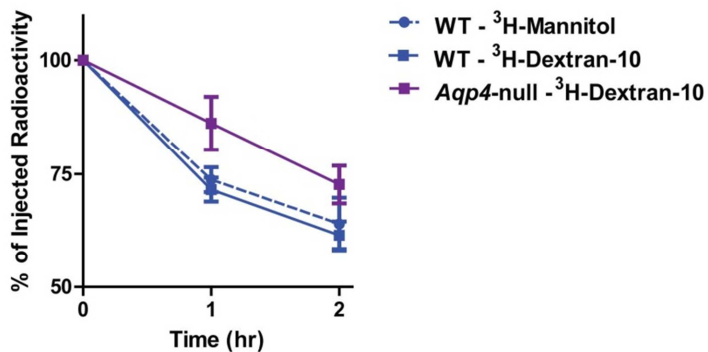


**(A-B)** Immunofluorescence labeling for AQP4 in the cortex of NG2-DsRed mice. Penetrating arteries are readily distinguished by intense, circumferential DsRed labeling of the vascular smooth muscle (A, empty arrowhead) while ascending veins exhibit irregular DsRed labeling (B, solid arrowhead). **(C)** Quantification of AQP4 immunoreactivity in perivascular endfeet, normalized to background AQP4 intensity. Periarterial endfeet expressed significantly less AQP4 than did pericapillary or perivenous endfeet (\* $P < 0.01$ , ANOVA;  $n=24$  arteries, 19 veins and 43 capillaries from 3 animals). **(D)** When AQP4 immunoreactivity was measured within  $20\mu\text{m}$  of the vessel wall (excluding the endfeet), periarterial AQP4 intensity was significantly reduced compared to levels around capillaries levels (\* $P < 0.05$ , t-test). This was largely driven by a subpopulation of penetrating arteries ( $\sim 40\%$  of overall group) that exhibited a marked absence of AQP4 immunoreactivity labeling for up to  $50\mu\text{m}$  surrounding the vessel (seen in A).

**Figure S8. Measurement of interstitial solute clearance from the brain.**

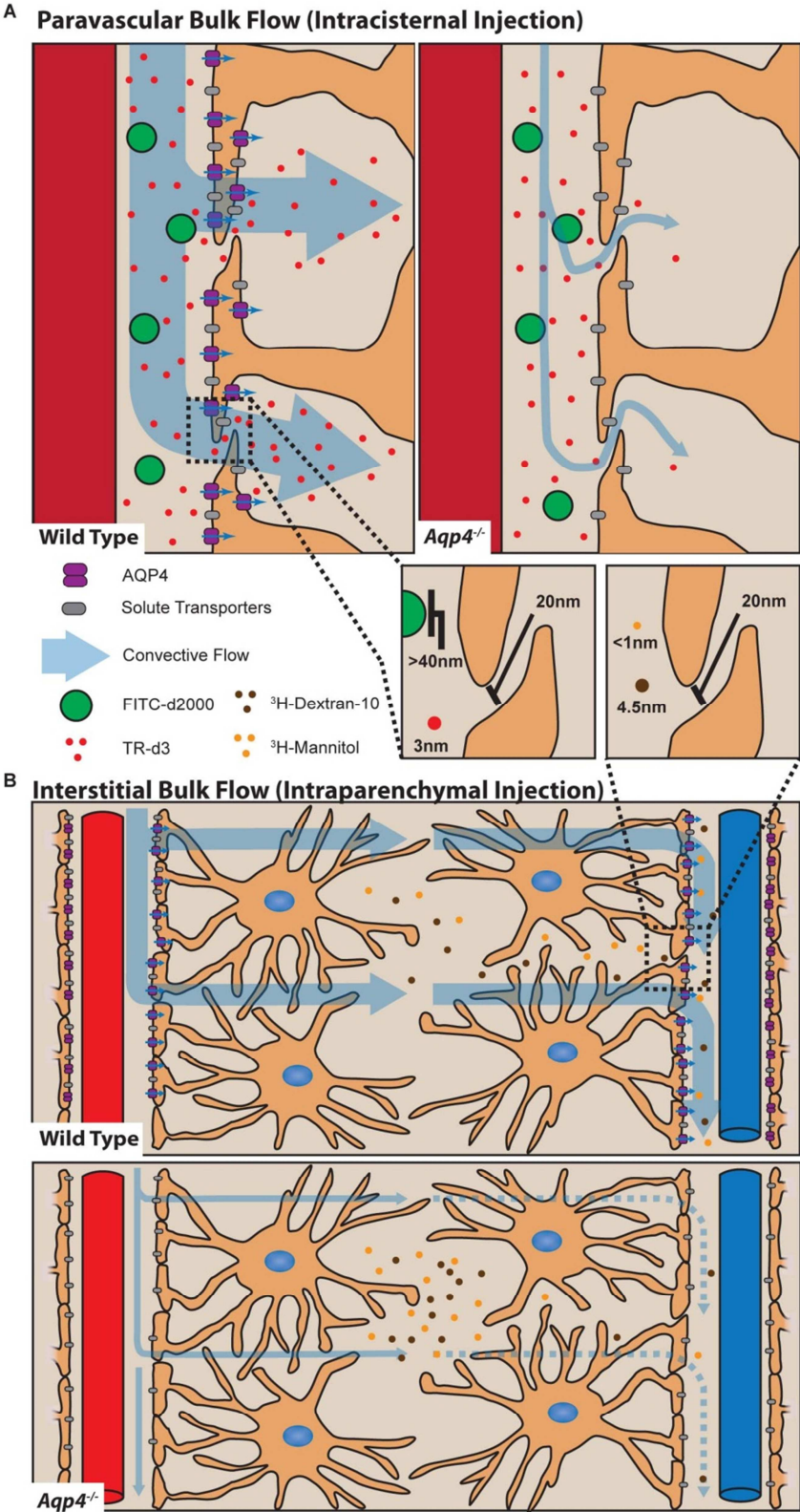


**B Brain  $^3\text{H}$ -Dextran-10 Clearance**



**(A)** Schematic diagram depicting the measurement of interstitial solute clearance from the brain parenchyma.  $^3\text{H}$ -mannitol,  $^3\text{H}$ -dextran-10 or  $^{125}\text{I}$ -amyloid  $\beta_{1-40}$  was injected into the striatum. To quantify radio-tracer clearance from the parenchyma, the brain was harvested at  $t=1$  or  $2$  hrs following radio-tracer injection. Brains were solubilized, then total brain radioactivity was measured by liquid scintillation counting. The remaining brain radioactivity ( $R'_{Brain}$ ) was calculated based upon the total measured brain radioactivity ( $R_{Brain}$ ) and the total injected radioactivity ( $R_{Inject}$ ). When the brain was harvested, the dura was removed. Thus the measured  $R_{Brain}$  value does not include radio-tracer present within the subarachnoid space. **(B)** The effect of *Aqp4* gene deletion upon the clearance of intra-parenchymally injected  $^3\text{H}$ -dextran-10 from the brain. In wild type animals, both  $^3\text{H}$ -mannitol and  $^3\text{H}$ -dextran-10 were cleared from the brain at identical rates. This is consistent with the observation that bulk flow [in contrast to diffusion(9)]-mediated transport is independent of molecular weight(4). *Aqp4* gene deletion had an effect upon the efflux of  $^3\text{H}$ -dextran-10 similar to that of  $^3\text{H}$ -mannitol (Fig. 5B), markedly reducing the rate of their clearance from the brain parenchyma (\* $P < 0.01$ ,  $n=4$  per time point).

Figure S9. Schematic diagram of paravascular and interstitial bulk flow pathways.



**(A)** Schematic depicting the proposed role of periarterial astroglial endfoot AQP4 in facilitating bulk water flow between the para-arterial influx pathway and the interstitial compartment. Because of high AQP4 expression, water passes freely across the perivascular endfoot. Small solutes, including the fluorescent tracer TR-d3 (MW 3kD), follow the resulting osmotic gradient into the interstitium through intercellular clefts between overlapping endfoot processes. Large solutes, including FITC-d2000 (MW 2000kD), cannot pass this cleft and are retained in the paravascular space. In *Aqp4*-null mice, water flux between the paravascular space and the interstitium is reduced, as is accompanying solute movement into the interstitium. Inset depicts physical dimensions of TR-d3, FITC-d2000 [ $d_H$ , hydration diameter (9)] and the inter-endfoot cleft (17). **(B)** Detailed schematic depicting the proposed role of astroglial AQP4 in maintaining convective ISF bulk flow and interstitial solute clearance. Para-arterial and paravenous AQP4 permits the free movement of water between the para-arterial influx and paravenous clearance pathway. This convective water flux sweeps interstitial solutes and tracers (such as  $^3\text{H}$ -mannitol and  $^3\text{H}$ -dextran-10) along its path. In *Aqp4*-null mice, water flux between the paravascular spaces and the interstitium are reduced, resulting in the failure of interstitial solute clearance. Inset depicts the physical dimensions of  $^3\text{H}$ -mannitol,  $^3\text{H}$ -dextran-10 and the inter-endfoot cleft. (See movie S2 for animation of this process)



**Movie S1. Time-lapse in vivo 2-photon imaging of para-arterial influx of intracisternal FITC-d40 into the mouse cortex.** Wild type mice were equipped with a cranial window with intact dura. The cerebral vasculature was visualized by intra-arterial Texas Red-d70 (70kD) injected via a femoral artery catheter. 10 $\mu$ l of FITC-d40 (1% in CSF) was injected intracisternally and tracer influx was imaged at the cortical surface, 60 and 120 $\mu$ m below the cortical surface at 1 min intervals (1min per frame). Video represents tracer influx over first 34 min post-injection. Note the tracer flux along the margins of cerebral surface arteries, followed by flux into the cortical parenchyma along penetrating arterioles. This is the first direct visualization of paravascular CSF influx into the brain parenchyma published.

**Movie S2. Animation depicting the role of paravascular CSF influx in interstitial solute clearance from the brain.**